

Nanomotion of Micro-Objects Driven by Light-Induced Elastic Waves on Solid Interfaces


Wei Lyu^{1,2,3}, Weiwei Tang,⁴ Wei Yan,^{2,3,*} and Min Qiu^{2,3,†}

¹Zhejiang University, Hangzhou, Zhejiang Province 310027, China

²Key Laboratory of 3D Micro/Nano Fabrication and Characterization of Zhejiang Province, School of Engineering, Westlake University, 18 Shilongshan Road, Hangzhou, Zhejiang Province 310024, China

³Institute of Advanced Technology, Westlake Institute for Advanced Study, 18 Shilongshan Road, Hangzhou, Zhejiang Province 310024, China

⁴College of Physics and Optoelectronic Engineering, Hangzhou Institute for Advanced Study, University of Chinese Academy of Sciences, No. 1, Sub-Lane Xiangshan, Xihu District, Hangzhou 310024, China

 (Received 9 October 2022; revised 5 January 2023; accepted 17 January 2023; published 17 February 2023)

It has been recently reported that elastic waves induced by nanosecond light pulses can be used to drive nanomotion of micro-objects on frictional solid interfaces, a challenging task for traditional techniques using tiny optical force. In this technique, the main physical quantities and parameters involved are temporal width and energy of light pulses, thermal heating and cooling time, friction force, and elastic waves. Despite a few experimental observations based on microfiber systems, a microscopic theory, which reveals how these quantities collaboratively enable motion of the micro-objects and derives what the underlying manipulation principles emerge, is absent. In this paper, a comprehensive theoretical analysis—centralized around the above listed physical quantities, and illuminated by a single-friction-point model in conjunction with numerical simulations—is established to pedagogically clarify the physics. Our results reveal the two essential factors in this technique: (1) the use of short light pulses for rapid thermal expansion overwhelming friction resistance and (2) the timescale asymmetry in thermal heating and cooling for accumulating a net sliding distance. Moreover, we examine the effects of spatially distributed friction beyond the single-friction-point consideration, and show “tug-of-war”-like friction stretching in the driving process. Given these insights, we positively predict that this elastic-wave-based manipulation principle could be directly translated to micro- and nanoscale optical waveguides on optical chips, and propose a practical design. We wish that these results offer theoretical guidelines for ongoing efforts of optical manipulation on solid interfaces with light-induced elastic waves.

DOI: [10.1103/PhysRevApplied.19.024049](https://doi.org/10.1103/PhysRevApplied.19.024049)

I. INTRODUCTION

Optical manipulation of micro- and nanoscaled objects provides substantial applications [1], such as single-cell analysis [2–4] and drug delivery [5,6] in micro-organism biology, atomic quantum processor [7,8] in physics, and microfluidic devices [9]. According to their different mechanisms and principles, the implementation routes of optical manipulations can be generally divided into optical tweezers using optical forces [10–12] or dielectrophoresis-based methods [13–17]. In all these techniques, it is crucial to mitigate adhesion between driven objects and their environments. Consequently, it is a common practice to carry out optical manipulation in liquids [9,18–20] or by levitating nanoparticles in vacuum [21–23], wherein the adhesion becomes negligible and smaller than pN—the typical order

of magnitude of optical and photophoretic forces [24–26] exerted on micro-objects.

Different from conventional routines, the researchers have recently proposed to exploit elastic waves induced by pulsed light to manipulate micro-objects. This opens up an alternative way to accomplish controllable and precise manipulation of micro-objects on solid interfaces, wherein the surface adhesion could easily exceed over μN [27]. The reported experiments, which are performed in microfiber-based systems using nanosecond pulsed light, are briefly summarized in Fig. 1 for clarification. The motion is stepwise driven by single pulses, and, in each step, the motion distance is only a few nanometers or even subnanometers. Consequently, the motion speed could be controlled by varying repetition rates and energy of laser pulses. Notably, several distinct nanomotion modules of gold microplates have been demonstrated, including in-plane rotation in the surface of the plate contacting with the microfiber [28], translation along azimuthal [29] or

*wyanzju@gmail.com

†qiumin@westlake.edu.cn

Schematic	Motion Module
	In-plane rotation in the surface of the plate contacting with the microfiber [28]
	Translation along azimuthal direction of the microfiber [29]
	Translation along axial direction of the microfiber [30, 31]
	Spiral motion combining both the azimuthal and axial translations [32]

FIG. 1. Existing experiments that report four motion modules of nanomotion of gold plates driven by elastic waves induced by nanosecond light pulses.

axial [30,31] direction of the microfiber, and spiral motion combining both the azimuthal and axial translations [32]. These different nanomotion modules can be controlled by carefully adjusting relative positions and contact configurations between the driven microplates and the microfibers, or by exploiting specific spatial profiles of optical absorption. For instance, the translation along the azimuthal direction of the microfiber requires the geometrical asymmetry in the two wings of the plate, and the motion is towards the short-wing side [29]. On the other hand, the translation along the axial direction of the microfiber requires either the asymmetry in the contact between the plate and the microfiber [32] or the profile asymmetry of the optical absorption profile [31], which, respectively, result in that the plate translates axially towards the contact side or the intense-absorption side. The combination of the azimuthal and axial translations gives the spiral motion. Lastly, the in-plane rotation is a consequence of the asymmetry in the two wings of the plate and the gradient distribution of the optical absorption power along the touching line between the plate and the microfiber [28].

These reported experiments of the elastic-wave-based nanomotion might inspire future developments of miniature motors on solid interfaces [33]. As a next step, a meaningful direction is to extend this technique from its initial micro-fiber-based system, e.g., to on-chip integration [34–39], therein bringing many unique applications. For instance, by manipulating motion modules and controlling precise positions of a micro-object in a waveguide network, one could potentially modulate light flow, and, thus, realize a mobile optical modulator or switch. In addition, by arranging relative positions of a group of micro-objects on a substrate, reconfigurable optical devices can

be achieved [40]. Plenty of experimental efforts are clearly demanded. Meanwhile, it is of equal significance to establish a comprehensive, rigorous understanding of the physical mechanism, and, further, to fairly access the features of this technique, as has been done for optical tweezers. This is the main purpose of this paper.

The current knowledge of the elastic-wave-based nanomotion considers dynamic interactions between elastic waves—due to temperature rising through optical absorption—and their induced friction force (the parallel component of surface adhesive force). The friction force is identified to drive the motion, similar to human walking. However, the existing knowledge is mainly proposed for phenomenologically interpreting the experimental observations, while being inefficient in quantitative predictions. This is because that the motion is a complicated optical-thermal-elastic process, wherein multiple physical parameters and quantities, such as temporal width and energy of light pulses, thermal heating and cooling time, friction resistance and elastic waves, are involved and couple with each other. Therefore, a precise, comprehensive understanding should necessarily take all these factors into account and classify their individual roles, which, however, still remains absent.

In this paper, we fill this gap by starting with a two-dimensional (2D) physical model, in which, a 2D plate on a substrate is driven by light pulses, as is shown in Fig. 2(a). Despite being slightly distant from the realistic experiments (summarized in Fig. 1), this designed physical model advantageously allows us to reveal the different roles of the key physical quantities through assisted analytic analysis. Along this way, we reveal how temporal width and energy of light pulses, thermal heating and cooling time, contact friction and its distribution impact the motion, and, further, how one could practically play these diverse factors benefiting the nanomotion. Particularly, to investigate interactions between friction force and light-induced elastic waves, a single-friction-point model is developed. These results are summarized in Secs. II–VI.

In Sec. VII, we provide perspectives for future developments of this technique and, particularly, discuss its practical realization on optical chips. We numerically evidence that a gold microplate can be driven on a Si_3N_4 nanowaveguide, where the friction force reaches tens of μN . Finally, Sec. VIII concludes the paper.

II. PHYSICAL PICTURE

The nanomotion of a micro-object driven by light-induced elastic waves hosts rich opto-thermo-elastic physics. A rigorous theoretical description should combine three sets of equations: Maxwell's equations, heat conduction equation, and elastic wave equation, from which meaningful quantifiers and relations—that specify, characterize the motion—might be derived. However, this

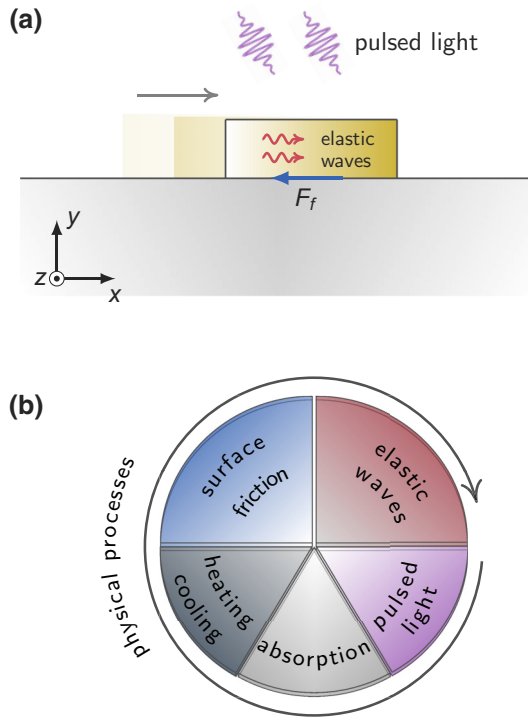


FIG. 2. (a) Sketch and (b) involved physical processes of nanomotion of a micro-object on a substrate driven by elastic waves induced by pulsed light.

approach is more suitable for numerical simulations, but difficult to bring analytic insights due to its mathematical complexity.

To bypass this technical difficulty, we omit less-useful physical details, and instead focus directly on the central physics: light-induced thermal deformation in the presence of surface friction. To put our strategy concretely, we recall the involved physical processes [see Fig. 2(b)]. First, under incidence of pulsed light, the micro-object converts light to heat. Then, the generated heat results in the temperature rising and excites elastic waves, therein leading to the thermal deformation of the micro-object. At the same time, the surface friction is induced to resist the deformation, and, counterintuitively drives the motion of the micro-object. Apparently, the last step, concerning the interplay between the surface friction and the deformation, is the key in the whole processes, in which, the explicit role of the surface friction could be quantized by contrasting the deformation of the micro-object with and without the friction. Then, the involved physical quantities and parameters can be dependably discussed around this friction-induced deformation difference. Moreover, to better interpret the physics, we intentionally refer to a simple 2D model [see Fig. 2(a)], as has been mentioned in the introduction.

Essential physical parameters—For a better clarification of the physical dynamics in the aforementioned

optical-thermal-elastic processes [see Fig. 2(b)], we introduce the following parameters:

(a) t_w and W_{abs} , temporal width and optical absorption energy of light pulses. In our study, light pulses are set to be Gaussian, and their temporal width t_w is defined to be $1/e$ width of the pulse energy.

(b) t_{heat} and t_{cool} , thermal heating and cooling time. With the use of short light pulses, t_{heat} is roughly about t_w . t_{cool} is defined as the time for the thermal energy decaying from peak to half.

(c) F_f^s , friction sliding resistance, which is the maximum allowable static friction exerted on the plate.

(d) v_L , velocity of excited elastic waves in the plate.

In addition to the above parameters, the other involved ones include $t_R \equiv 2L_p/v_L$, one-round-trip travel time of the elastic waves in the plate, where L_p denotes the plate length in the x direction [see Fig. 2(a)]; $t_{\text{diff}} \equiv L_p^2/\alpha_{\text{diff}}$, characteristic time for heat spreading through the plate, where α_{diff} denotes the thermal diffusivity; $\lambda_{\text{el}} \equiv v_L t_w$, characteristic wavelength of the excited elastic waves.

To have a concrete perception of these parameters, we estimate their magnitudes by considering a gold plate with $L_p = 10 \mu\text{m}$ (typical length size of the micro-object used in the existing experiments of the nanomotion [28–30,32]). For gold, $v_L \sim \sqrt{E/\rho}$ (E , Young’s modulus; ρ , mass density) is about 2000 m/s and $\alpha_{\text{diff}} = \sqrt{k/\rho c_p} \simeq 10^{-4} \text{ m}^2/\text{s}$ (k , thermal conductivity; c_p , specific heat capacity). Consequently, there are $t_R \simeq 10 \text{ ns}$ and $t_{\text{diff}} \simeq 100 \text{ ns}$. We thus observe that $t_R \ll t_{\text{diff}}$, that is, the elastic waves travel much faster than the heat diffusion. This relation implies that the object can be well deformed by the elastic waves at positions where the heat has not been yet spread. This observation leads us to the following deduction: the traditional picture of “static” thermal expansion and contraction, which is widely used for describing thermal deformation, is incomplete in the nanosecond regime, and the elastic waves should be taken into account.

t_{cool} , the cooling time, is mainly determined by the heat conduction from the plate into the substrate, which could vary from tens to thousands (or even more) of nanoseconds, depending on the thermal contact (see latter discussions concerning Fig. 3). t_w , pulse duration, on the other hand, is an external parameter relating to the laser source used, which determines the heating time, t_{heat} . With t_w in the order of nanoseconds, the characteristic wavelength of the excited elastic waves, λ_{el} , is estimated from its definition to be in the order of micrometers.

In the reported experiments where gold plates contact with microfibers with diameter of a few microns, the sliding resistance, F_f^s , is measured to be a few μN [29,31]. It is known that the F_f^s is linearly proportional to the contact area. The contact area between the gold microplate and the microfiber with diameter of a few microns is estimated to

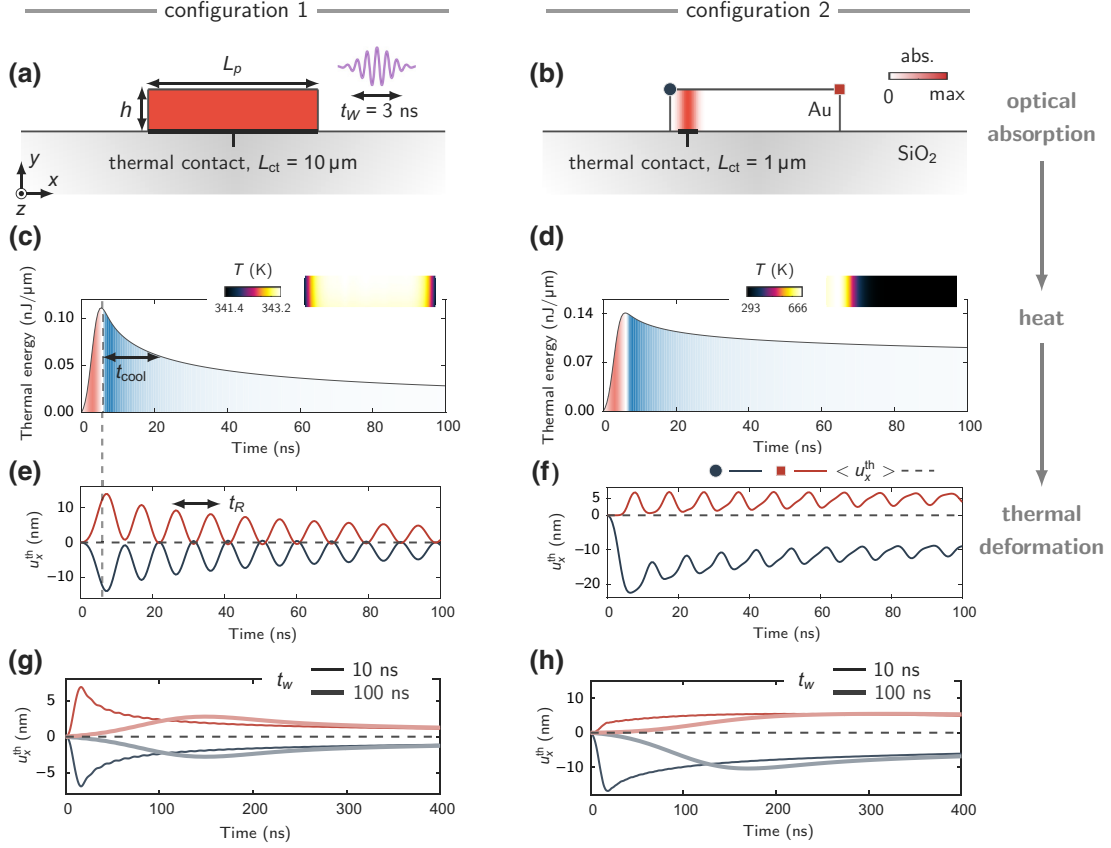


FIG. 3. Thermal deformation without friction driven by a nanosecond light pulse. (a),(b) Schematics of two studied configurations: (a) uniform optical absorption in a gold microplate with a full thermal contact between the plate and the SiO₂ substrate; (b) localized optical absorption with a partial thermal contact. The 2D plate in the x - y plane has length and height of $L_p = 10 \mu\text{m}$ and $h = 50 \text{nm}$, respectively. In (b), the optical absorption has a Gaussian distribution in the x direction, centered at $1 \mu\text{m}$ from the left edge of the plate, with $1/e$ width $1 \mu\text{m}$; the thermal contact length is $1 \mu\text{m}$ with its center coinciding with that of the optical absorption. (c),(d) Temporal evolutions of the thermal energy stored in the plate, highlighting the heating (red shaded areas) and cooling phases (blue shaded areas). Insets: temperature profiles of the plate at the peak of the thermal energy, $t = 6 \text{ns}$. (e),(f) Temporal evolutions of (dominant) x -component elastic displacements induced by the temperature variation, u_x^{th} , of two edge points [red and blue lines; edge points are marked in (b)], and of x -component centroid displacement, denoted by $\langle u_x^{\text{th}} \rangle$ (dashed lines). In (c)–(f), the temporal width of the light pulse is $t_w = 3 \text{ns}$ and the total optical absorption energy is $W_{\text{abs}} = 0.2 \text{nJ}/\mu\text{m}$. Note the peak of the stored thermal energy is observed to be less than $W_{\text{abs}} = 0.2 \text{nJ}/\mu\text{m}$ due to the heat conduction from the plate into the substrate. The simulations are performed with COMSOL Multiphysics, and the material parameters are taken from the built-in MEMS library of COMSOL Multiphysics (see Table S1 within the Supplemental Material [41]). (g),(h) Same as (e),(f), except that temporal widths of light pulses increases to $t_w = 10, 100 \text{ns}$.

be in the order of $10 \mu\text{m} \times 10 \text{nm}$, where $10 \mu\text{m}$ denotes the typical contact length along the axial direction of the microfiber, and 10nm is the order of the transverse contact length that is calculated from the contact simulations considering the interfacial van der Waals forces (see Fig. S1 within the Supplemental Material [41]).

III. THERMAL DEFORMATION WITHOUT FRICTION IN THE NANOSECOND REGIME

A. General features

We start by studying thermal deformation of a micro-object in the absence of surface friction under incidence of a single light pulse. The micro-object responds to

the light-induced temperature change δT and deforms its shape. The deformation is characterized by the coordinate changes of the structure, denoted by $\mathbf{u}^{\text{th}}(\mathbf{r}; t)$ (termed as elastic displacements hereafter), which satisfy [42]

$$\begin{aligned} \nabla \times \nabla \times \mathbf{u}^{\text{th}}(\mathbf{r}; t) - 2 \frac{1 - \sigma}{1 - 2\sigma} \nabla \nabla \cdot \mathbf{u}^{\text{th}}(\mathbf{r}; t) \\ + 2\alpha_{\text{th}} \frac{1 + \sigma}{1 - 2\sigma} \nabla \delta T(\mathbf{r}; t) \\ + \frac{2\rho(1 + \sigma)}{E} \frac{\partial^2 \mathbf{u}^{\text{th}}(\mathbf{r}; t)}{\partial t^2} = 0. \end{aligned} \quad (1)$$

Here σ , E , and α_{th} , respectively, denote Poisson's ratio, Young's modulus, and the coefficient of linear thermal

expansion of the micro-object. The temperature change δT relates to the optical absorption. The temperature evolution undergoes heating phase during the short period of the pulse injection and the next cooling phase, during which the object successively expands and contracts its volume.

In the absence of the surface friction (interfacial force), the external force exerted on the micro-object is null. Consequently, although the elastic displacements \mathbf{u}^{th} exist, their spatial average (i.e., the centroid displacement) remains zero. The object is thus “motionless”. This can be examined by applying the volume integration to Eq. (1), wherein its first three terms of the left side vanish, thus leaving $\partial^2 \langle \mathbf{u}^{\text{th}}(t) \rangle / \partial t^2 = 0$ with $\langle \mathbf{u}^{\text{th}}(t) \rangle$ denoting the spatial average of $\mathbf{u}^{\text{th}}(\mathbf{r}; t)$.

With the use of (nanosecond) pulsed light, as has been discussed in Sec. II, a complete description of the thermal deformation should take dynamic elastic-wave propagations into account, since $t_R \ll t_{\text{diff}}$. Referring to the studied 2D plate, the excited elastic waves are mainly carried by the fundamental longitudinal mode, with elastic displacements pointing along the propagation direction and uniformly distributing over the plate thickness. Specifically, the wave number k_L and velocity v_L of the fundamental longitudinal mode are given by [32]

$$k_L = \omega \sqrt{\rho(1 - \sigma^2)/E}, \quad v_L = \sqrt{E/(\rho(1 - \sigma^2))}. \quad (2)$$

Note that Eq. (2) is valid under the assumption that $k_L h \ll 2\pi$ (h , plate thickness).

We numerically illustrate the general features of the light-pulse-induced thermal deformation in Fig. 3. A gold 2D plate with thickness $h = 50$ nm and length $L_p = 10$ μm is placed on a glass substrate. A Gaussian light pulse, with temporal width $t_W = 3$ ns, is injected into the plate and leads to an absorption energy of $W_{\text{abs}} = 0.2$ nJ/ μm (note that the unit of W_{abs} is nJ/ μm due to the consideration of the 2D plate). We consider two representative configurations of the absorption distributions, (1) evenly and (2) locally distributed along the length direction (i.e., x direction) of the plate, as is shown in Figs. 3(a) and 3(b), respectively, and their spatial distributions are described in the figure caption. Moreover, two different thermal contact scenarios are set to examine the effect of the cooling time t_{cool} on the deformation. In the first case [Fig. 3(a)], the plate and the substrate are assumed to be in full thermal contact, so that the thermal energy in the plate could be rapidly conducted into the substrate. In contrast, the other case [Fig. 3(b)] models the slow cooling, where the plate and the substrate has a short thermal contact length of 1 μm (see the figure caption for more details). The thermal contact length practically relates to the surface topography of the plate [32]. The full contact is realizable when the plate is flat and the associated roughness is negligible, otherwise, the partial contact occurs.

B. Heat evolution

Figures 3(c) and 3(d) plot the temporal evolutions of the thermal energy stored in the plate. Note the peak of the stored thermal energy is observed to be less than $W_{\text{abs}} = 0.2$ nJ/ μm due to the heat conduction from the plate into the substrate. In the full-contact case [Fig. 3(c)], the thermal energy quickly drops after peak due to the efficient heat conduction from the plate into the substrate. The cooling time t_{cool} is estimated to be only about 10 ns. In contrast, in the partial-contact case [Fig. 3(d)], the heat-conduction channel between the plate and the substrate is narrow, such that the cooling process exhibits a much longer tail with t_{cool} exceeding over 100 ns.

The temperature distribution in the plate is the joint result of the optical absorption distribution and the heat diffusion. In the early period with $t \ll t_{\text{diff}}$ ($t_{\text{diff}} \simeq 100$ ns, time for heat fully diffusing the entire plate), the heat localizes around where the optical absorption takes place, and the temperature distribution resembles the absorption distribution, as shown in the insets of Figs. 3(c) and 3(d).

C. Thermal deformation

Figures 3(e) and 3(f) trace the dominant x -component elastic displacements, u_x^{th} , of the left (dark blue lines) and right (dark red lines) ending points [marked in Fig. 3(b)] of the plate. Note that, since we here consider a thin plate with thickness only about tens of nanometers, the deformation in the thickness direction is almost uniform. It is seen that u_x^{th} oscillates with periodicity close to the one-round-trip travel time of the elastic waves ($t_R \simeq 10$ ns), which evidences the propagation of the elastic waves. Moreover, as indicated in Eq. (1), the thermal deformation is directly determined by the temperature profile. In this regard, with a uniform temperature distribution, the left and right halves of the plate deform symmetrically, as verified in Fig. 3(e) that u_x^{th} of the left and right endpoints show the same magnitude but opposite signs. In contrast, if the temperature distribution is nonuniform, so is the deformation, i.e., featuring the asymmetric deformation, as is confirmed in Fig. 3(f).

During the period of the light pulse injection [the left regions bounded by the vertical dashed lines in Figs. 3(c) and 3(e)], the thermal deformation rapidly intensifies to its maximum as the thermal energy climbs to the peak. Then, the thermal cooling initiates and the deformation gradually mitigates. The recovery rate of the deformation is determined by t_{cool} : a smaller value of t_{cool} (i.e., faster thermal cooling) results in a faster deformation recovery and vice versa. Furthermore, regardless of the dynamic change of the local deformation, the plate centroid always remains zero [see the horizontal dashed curves in Figs. 3(e) and 3(f)], since no external force is applied.

The temporal width of the light pulse t_W also affects the thermal deformation. To illustrate this effect, we increase

t_W to 10 and 100 ns. The computed x -component elastic displacements, u_x^{th} , as functions of time, are plotted in Figs. 3(g) and 3(h). Markedly, as t_W increases, the deformation oscillations become apparently weaker. This is because that the adjacent oscillations with the interval t_R , due to the round trips of the elastic waves, are smeared out in a longer period of t_W when the elastic waves are continuously excited. Given this intuition, we deduce that the visibility of the deformation oscillations requires that $t_W < t_R$ ($t_R \simeq 10$ ns here), as is confirmed by comparisons between Figs. 3(e)–3(f) and 3(g)–3(h). Moreover, in the heating period, we find that the deformation speed ($\partial u_x^{\text{th}}/\partial t$) increases as t_W decreases. However, in the cooling period, the rate of the deformation recovery is independent of t_W , and is instead determined by t_{cool} , as is seen in Figs. 3(e)–3(h) that the decaying tails of u_x^{th} are similar for t_W with different values.

IV. ACCOUNTING SURFACE FRICTION IN THERMAL DEFORMATION: SINGLE-FRICTION-POINT MODEL

A. Introduction of single-friction-point model

The friction force exerts on the plate when the latter slides on the substrate. To elucidate the effects of the friction on the thermal deformation, we establish a simplified physical model by assuming that the contact length along the sliding direction of the micro-object is significantly smaller than both the wavelength of the excited elastic waves λ_{el} and the plate length L_p , so that the friction force can be approximated by a point force. This simplification not only brings analytic insights, but also has practical relevancy. For instance, in the existing experiment that the gold microplate azimuthally moves around the microfiber [29], where the contact length in the azimuthal direction is negligible, as is shown in the left panel of Fig. 4, this single-friction-point model (SFPM) captures the real physics. Admittedly, there are cases where the SFPM is defective, e.g., when studying that a flat microplate translates along the axial direction of a microfiber, as is shown in the right panel of Fig. 4. Then, the spatial distribution of the friction force is expected to play a role, for which the simplest extension is to consider two friction points, as shown in the right panel of Fig. 4 (see more discussions in Sec. VI).

B. Derivations of SFPM

Consider that a point-friction force, denoted by F_f , is applied to the plate at $x = x_0$. The F_f , similar to the temperature variation δT , also induces the deformation of the plate. In the nanosecond regime and at microscales, the friction-induced elastic displacements also have to be evaluated from the elastic wave equation. Specially, the induced dominant x -component elastic displacement, u_x^f ,

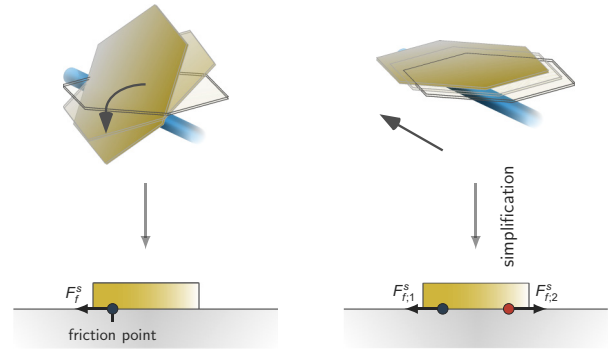


FIG. 4. Intuitive simplifications of complex contact scenarios to single friction-point (left) and two friction points (right). The single-friction-point model well approximates the case where the contact length in the motion direction is negligible, such as that the azimuthal movement of a gold microplate around the microfiber [29]. On the other hand, the two friction points are introduced for the case when the contact length in the motion direction becomes noticeable comparing to the characteristic elastic wavelength or the object dimension, such as the axial movement of the plate along the microfiber [30,31].

is formulated as

$$u_x^f(x, t) = \int_{-\infty}^t G_{\text{el}}(x, x_0; t - t') F_f(t') dt', \quad (3a)$$

where $G_{\text{el}}(x, x_0; t - t')$, Green's function of the linear elastic equation (see Technical Note within the Supplemental Material for its definition [41]), can be expanded by the fundamental longitudinal elastic modes [i.e., Eq. (2)], and is given by

$$G_{\text{el}}(x, x_0; t - t') \simeq \frac{t_R}{4M_p} \sum_{s=0}^3 \sum_{n=0}^{\infty} H(t - t' - t_s - nt_R). \quad (3b)$$

Here, M_p denotes the mass of the 2D plate; t_s 's ($s = 0, 1, 2, 3$) denote the travel time of the elastic waves from x_0 to the point x four times in one round trip, with $t_0 = |x - x_0|/v_L$, $t_1 = t_R - |x - x_0|/v_L$, $t_2 = |L_p - x - x_0|/v_L$, and $t_3 = |L_p + x + x_0|/v_L$; $H(t)$ is the Heaviside step function with $H(t) = 1$ for $t \geq 0$ and $H(t) = 0$ otherwise; $n = 0, 1, 2, 3, \dots$ label the round trips of the elastic waves bouncing back and forth inside the plate. The validity of Eq. (3b) is numerically confirmed in Fig. S2 within the Supplemental Material [41]. The y dependencies in Eq. (3a) and (3b) are dropped since we here consider thin microplates with thickness significantly smaller than micrometers and the elastic displacements are approximately uniform in the thickness direction, as is validated numerically in Figs. 5(b2) and 8(d2).

Interestingly, Eq. (3a) can be reformulated to our familiar Newtonian second law when F_f is a slowly varying

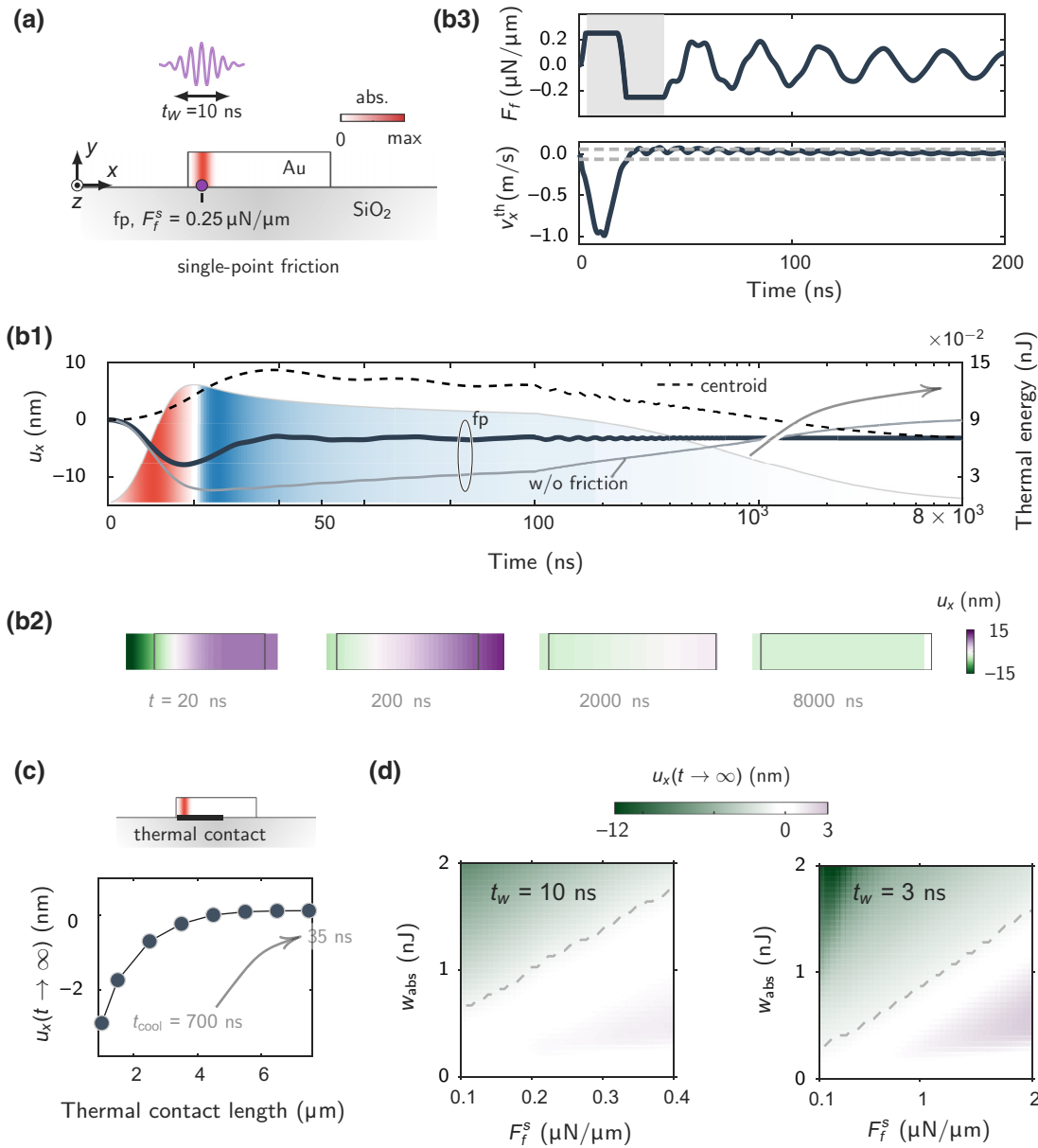


FIG. 5. Sliding dynamics with a single friction point driven by a nanosecond light pulse. (a) Sketch of the investigated problem, which adds a point friction at $1\ \mu\text{m}$ from the left edge of the plate to the “configuration-2” system studied in Fig. 3. (b1) Temporal evolutions of thermal energy (shaded area), and x -component elastic displacements of the friction point (solid lines) and the plate centroid (dashed line). (b2) Profiles of x -component elastic displacements at different times $t = 20, 200, 2000, 8000\ \text{ns}$. (b3) Temporal evolutions of x -component friction force (upper panel) and thermal deformation velocity (lower panel) of the friction point. The gray area in the upper panel marks the sliding period, while the dashed lines in the lower panel mark the predicted sliding threshold velocity v^s . In (b1)–(b3), the injected light pulse has $t_w = 10\ \text{ns}$ (temporal width) and $W_{\text{abs}} = 0.2\ \text{nJ}/\mu\text{m}$. The friction point has $F_f^s = 0.25\ \mu\text{N}/\mu\text{m}$. (c) Net sliding distance as a function of the thermal contact length. As the thermal contact length increases from $1\ \mu\text{m}$ [that is in (b1)–(b3)] to $7.5\ \mu\text{m}$, the cooling time decreases from 700 to 35 ns. (d) Net sliding distances as functions of the optical absorption energy W_{abs} and friction resistance F_f^s for $t_w = 10\ \text{ns}$ (left panel) and $t_w = 3\ \text{ns}$ (right panel). The dashed lines trace the sliding distance of $-1\ \text{nm}$ in the $W_{\text{abs}} - F_f^s$ parameter space. The other simulation settings in (d) are the same as in (b1)–(b3).

function in t_R . In this case, the round-trip series can be approximate by integrals over time, so that there is $u_x^f = \int_{-\infty}^t \int_{-\infty}^{t'} F_f(t'')/M_p dt'' dt'$, which is just the integral form of Newton’s second law.

The friction force F_f depends on the elastic displacement induced by the temperature change δT , denoted by u_x^{th} [see Eq. (1)] and also on itself at the previous time. To reveal this dependence, we decompose u_x^f into the

direct propagation term $u_{x;0}^f$ and the remaining reflection term $u_{x;R}^f$: $u_{x;0}^f = t_R/(4M_p) \int_{-\infty}^t H(t-t-t_0)F_f(t')dt'$ and $u_{x;R}^f = u_x^f - u_{x;0}^f$. The total x component elastic displacement u_x , including both thermal and friction contributions, is $u_x = u_{x;0}^f + u_{x;R}^f + u_x^{\text{th}}$. Next, to eliminate the integrals in u_x^f , we employ the time derivative to u_x and introduce the deformation velocity $v_x \equiv \partial u_x / \partial t$. On the friction point ($x = x_0$), we have that

$$v_x(x_0; t) = v_{x;0}^f(x_0; t) + v_{x;R}^f(x_0; t) + v_x^{\text{th}}(x_0; t), \quad (4a)$$

with

$$v_{x;0}^f(x_0; t) = \frac{t_R}{4M_p} F_f(t), \quad (4b)$$

and $v_{x;R}^f(x_0; t) = t_R/(2M_p) \sum_{n=1}^{\infty} F_f(t - nt_R) + t_R/(4M_p) \sum_{s=2}^3 \sum_{n=0}^{\infty} F_f(t - nt_R - t_s)dt'$ depending on F_f at the previous time.

In Eq. (4a), the instantaneous effect of the friction force on the elastic displacement is to induce $v_{x;0}^f$ to cancel with $v_{x;R}^f + v_x^{\text{th}}$, thus minimizing the magnitude of v_x . Specifically, when the friction point is still ($v_x = 0$), we have $F_f = -4M_p(v_{x;R}^f + v_x^{\text{th}})/t_R$, which gives the expression of the static friction force. Besides, it is known that the static friction force is bounded by $|F_f| \leq F_f^s$, where F_f^s is the sliding resistance. When this bounding condition is broken, it means that the friction point slides, and, then, the dynamic friction force $F_f = -\text{sgn}(v_x)F_f^d$ exerts on the plate, where $\text{sgn}(v_x) = \pm 1$ for $v_x > 0$ and $v_x < 0$, respectively. Note that the dynamic friction force F_f^d is generally different from F_f^s . Nevertheless, for convenience of our analysis, we here simply put $F_f^d = F_f^s$.

Given the above physical arguments, a strategy to determine the friction force is formulated as follows:

$$F_f = -4M_p(v_{x;R}^f + v_x^{\text{th}})/t_R \quad (5a)$$

if $|F_f| < F_f^s$, i.e., $|v_{x;R}^f(t) + v_x^{\text{th}}(t)| < F_f^s t_R / 4M_p$;

$$F_f = -\text{sgn}[v_{x;R}^f + v_x^{\text{th}}]F_f^s, \quad (5b)$$

otherwise.

V. EFFECTS OF FRICTION ON THERMAL DEFORMATION: INSIGHTS FROM BORN APPROXIMATION OF SFPM

A. Born approximation

Equations (3a)–(3b) self-consistently define the SFPM, which can be immediately applied for numerical simulations. However, their use in analytic analysis is still hindered by the fact that the friction force at time t correlates

with itself at the previous time. To remove this difficulty, we assume $|v_{x;R}^f| \ll |v_x^{\text{th}}|$, and, accordingly, neglect $v_{x;R}^f$ in Eqs. (4a). This approximation spiritually resembles the so-called Born approximation in the quantum wave-scattering theory [43], where the leading-order wave scattering due to the incident waves (which, in our case, is parameterized by $u_{x;0}^f$) is considered to be dominant, while the higher-order scattering terms (which here represent the elastic waves induced by the friction force at the previous time, $u_{x;R}^f$) are dropped. In the heating period when the thermal deformation significantly dominates over the friction, this approximation is proper. However, in the cooling period when the thermal deformation mitigates, v_x^{th} and $v_{x;R}^f$ could become comparable, making the approximation invalid. Nevertheless, this invalidity should not bring serious effect on our qualitative understanding of the deformation dynamics, as long as the deformation mainly takes place in the intense-thermal-deformation period, which is particularly true with the use of short nanosecond laser pulses. Bearing these facts in mind, we proceed to derive the consequences of the Born approximation, which are supported by the full-numerical results.

Under the Born approximation, the strategy to determine the friction force, formulated in Eqs. (5a) and (5b), could be simplified to $F_f \simeq -4M_p v_x^{\text{th}}/t_R$, when $|v_x^{\text{th}}| < v^s$ with $v_x = 0$; $F_f(t) \simeq -\text{sgn}[v_x^{\text{th}}(t)]F_f^s$ when $|v_x^{\text{th}}| > v^s$ with $v_x \simeq v_x^{\text{th}} - \text{sgn}[v_x^{\text{th}}(t)]v^s$. Here, the threshold velocity v^s , which defines the minimum magnitude of the thermal deformation velocity required to enable the motion of the friction point, is given by

$$v^s = \frac{F_f^s t_R}{4M_p}. \quad (6a)$$

And the sliding distance of the friction point is

$$u_x(t) \simeq \int_{-\infty}^t (v_x^{\text{th}}(t') - \text{sgn}[v_x^{\text{th}}(t')]v^s)H(|v_x^{\text{th}}(t')| - v^s)dt', \quad (6b)$$

where $H(x)$ is the Heaviside step function that is defined below Eq. (3b).

B. Implications from Eqs. (6)

(1) To realize a large sliding distance, it is necessary to enlarge the asymmetry in the heating and cooling timescales. Otherwise, v_x^{th} in the heating and cooling periods, intend to cancel each other in Eq. (6b), thus reducing the net sliding distance. This requires either $t_{\text{heat}} \gg t_{\text{cool}}$ or $t_{\text{heat}} \ll t_{\text{cool}}$. The former condition $t_{\text{heat}} \gg t_{\text{cool}}$ demands the use of a pulse with the rising time much longer than t_{cool} . At the same time, the cooling should be fast enough to make thermal deformation velocity v_x^{th} exceed v^s . On the other hand, the condition $t_{\text{heat}} \ll t_{\text{cool}}$ can be much more

easily met by using a short light pulse with $t_w \ll t_{\text{cool}}$ (note that the heating timescale t_{heat} is determined by t_w), which we focus on in the present paper.

Having the timescale asymmetry between the heating and cooling periods, the sliding distance, approximated with Eq. (6b), is mainly contributed from the dominant thermal phase, which has a larger magnitude of v_x^{th} . The stabilized sliding distance as $t \rightarrow \infty$ is then expected to point in the same direction as the thermal deformation in the dominant thermal phase.

(2) To realize sliding against a larger friction, it is better to use shorter light pulses (with smaller t_w) than longer ones. This is because to enable the motion of the friction point, the magnitude of the thermal deformation velocity v_x^{th} should exceed the threshold velocity v^s , otherwise, the friction point remains still. This prerequisite calls for a rapid thermal deformation, which mainly occurs in the heating period due to our consideration $t_{\text{heat}} \ll t_{\text{cool}}$ (see the above discussions about the first implication). Specifically, considering the existing experiments summarized in Fig. 1, where the typical size of the gold plate is approximately $10 \mu\text{m} \times 10 \mu\text{m} \times 50 \text{nm}$, indicating that $M_p \sim 10^{-13} - 10^{-12} \text{kg}$ and $t_R \sim 10 \text{ns}$; moreover, it has been measured that $F_f^s \sim \mu\text{N}$ [29,31]. Thus, from Eq. (6a), the threshold velocity v_x^s is inferred to be in the order of cm/s. As is shown in Fig. 3, with the use of the nanosecond pulsed light, u_x^{th} rapidly varies within the heating period, when v_x^{th} can easily approach the order of m/s, significantly exceeding v^s . In contrast, if continuous light is used, the related thermal deformation is gentle, and the nanomotion disappears, which has been validated experimentally [28,29]. Furthermore, as t_w decreases, the thermal deformation velocity v_x^{th} (in the heating period) increases, thus making it easier to exceed the threshold velocity v^s . Below, our numerical studies mainly focus on the use of nanosecond pulsed light echoing the same choice in the existing experiments [28,29,31,32]. Nevertheless, as implied by our theoretical analysis, the use of shorter short light pulse, such as picosecond and femtosecond laser pulses, is also possible, which deserves further experimental explorations.

C. Numerical validations

We numerically validate the aforementioned implications by revisiting the numerical case ‘‘configuration 2’’ studied in Fig. 3. A point friction force with $F_f^s = 0.25 \mu\text{N}/\mu\text{m}$ (note that the unit of F_f^s is $\mu\text{N}/\mu\text{m}$ due to the 2D nature of the plate) is introduced at the center of the thermal contact, a light pulse with temporal width $t_w = 10 \text{ns}$ and absorption energy $W_{\text{abs}} = 0.2 \text{nJ}/\mu\text{m}$ is used, as is sketched in Fig. 5(a) (see the figure caption for more details). The numerical computations are implemented by using Eqs. (3a)–(4a) to exactly include the friction

contributions (see Technical Note within the Supplemental Material for details of numerical implementations [41]).

The shaded region in Fig. 5(b1) illustrates the temporal evolution of the thermal energy, which features the asymmetry in the heating and cooling timescales, i.e., fast heating and slow cooling. The dark solid line in Fig. 5(b1) plots the temporal evolution of the x -component elastic displacement of the friction point, u_x . It shows that the friction point mainly slides in the heating period, when the thermal deformation is intense, while mildly moving in the cooling period, when the thermal deformation is gentle. As a result, as $t \rightarrow \infty$, the plate accumulates a negative sliding distance, consistent with the observation from the Born approximation. In contrast, without the friction, the friction point returns back to its original position by the slow thermal contraction, and the net sliding distance is zero, as is illustrated by the gray solid line in Fig. 5(b1).

For a better visualization of the sliding dynamics, we plot the friction force F_f and the thermal deformation velocity v_x^{th} as functions of time in Fig. 5(b3). The sliding period is outlined by the shaded regions in the upper panel of Fig. 5(b3), where the magnitude of the friction force is equal to $F_f^s = 0.25 \mu\text{N}/\mu\text{m}$. Particularly, in the heating period, the sliding is along the $-\hat{x}$ direction and the friction force is thus positive. Notably, it appears when $|v_x^{\text{th}}| > v^s$ [see the lower panel of Fig. 5(b3) where the dashed lines mark $|v_x^{\text{th}}| = v^s$], as predicted from the Born approximation. In contrast, in the early cooling period, the sliding is along the \hat{x} direction and the friction force becomes negative. In this period, due to the negligible magnitude of v_x^{th} , the contribution from the friction force at the previous time [characterized by $v_{x;R}^f$ in Eq. (3b)] becomes relatively significant and, thus, the Born approximation is defective. As a result, the sliding condition is no longer described by $|v_x^{\text{th}}| > v^s$.

We also evaluate the x -component centroid displacement of the plate [denoted by $\langle u_x \rangle$; see dashed line Fig. 5(b1)] with Newton’s second law $M_p \partial^2 \langle u_x \rangle / \partial t^2 = F_f$. It is initially in the opposite direction to the displacement of the friction point, and then gradually approaches the latter. This can be understood by examining the temporal evolution of the friction force, as is shown in the upper panel of Fig. 5(b3). Further, as is plotted in Fig. 5(b2), the profiles of the x -component elastic displacements of the plate at $t = 20, 200, 2000, 8000 \text{ns}$ show that the left and right sides of the plate are initially stretched in opposite directions by the thermal deformation, and then, the two sides gradually crawl toward the friction point that is anchored by the friction force. Finally, the entire plate gets the same displacement.

We next illustrate the effects of the thermal asymmetry by varying the cooling time t_{cool} , while maintaining other parameters unchanged. The cooling time is modified by changing the thermal contact length between the plate and

the substrate, as illustrated in the inset of Fig. 5(c). Initially, this length [as in Fig. 3(b)] is $1 \mu\text{m}$ that leads to $t_{\text{cool}} \simeq 700$ ns. Increasing it to $7.5 \mu\text{m}$, t_{cool} is reduced to 35 ns, close to $t_w = 10$ ns. As is discussed above, the intensified thermal cooling, which reduces the thermal asymmetry, drags the friction point more back to its initial position in the cooling period, thus decreasing the net sliding distance, as is confirmed in Fig. 5(c).

Further, we study the benefits of using shorter light pulses to overcome greater friction. By varying the injected optical absorption energy W_{abs} and the sliding resistance F_f^s [the other parameters are set as the same as in Figs. 5(b1)–(b3)], the net sliding distances for $t_w = 3, 10$ ns are plot in Fig. 5(d). The results show that, under the injection of a small amount of nanojoule absorption energy, the shorter pulse with $t_w = 3$ ns can enable the sliding of the plate under larger friction resistance than the longer pulse with $t_w = 10$ ns. This fact can be more clearly appreciated by observing the dashed lines in Fig. 5(d), which mark an exemplified sliding distance of -1 nm and show that the same sliding distance is achieved under a larger friction with the use of a shorter pulse. Moreover, we note that, in most of the area of the simulated $W_{\text{abs}} - F_f^s$ parameter space, the sliding distance is negative (green color). This agrees with the insight from the Born approximation that the plate slides along the same direction as the thermal deformation of the friction point in the heating period. However, there exist also small purple regions, showing the positive sign of the sliding distance. This “contradiction” manifests the failure of the Born approximation, and occurs when the friction-induced elastic waves become comparable to the thermal-induced ones.

VI. BEYOND SINGLE-FRICTION-POINT MODEL: EFFECTS OF FRICTION DISTRIBUTION

As the friction dimension along the sliding direction increases, the spatial distribution of the friction force, beyond the single-point-friction consideration, needs to be taken into account. To illustrate this effect, the simplest extension is to introduce two friction points and study their joint effects on the thermal deformation. Practically, referring to a flat or partially curved plate on a substrate, as is sketched in the right panel of Fig. 4, this extension could be regarded as a crude approximation to the real continuous contact by dividing the contact region in half and concentrating the friction force in each half into a point force.

A. Case I

First, to establish a link with the SFPM, we split the single friction point in Fig. 5 into two with a small separating distance of $1 \mu\text{m}$. The sliding resistances of two points are set to be $F_{f;1}^s = F_{f;2}^s = 0.125 \mu\text{N}/\mu\text{m}$, as is sketched in Fig. 6(a). In this case, the distance between the two points

is significantly smaller than the plate length, so that their thermal deformation properties are expected to be similar. Moreover, their distance is also smaller than the characteristic elastic wavelength $\lambda_{\text{el}} = t_w v_L \simeq 20 \mu\text{m}$ ($t_w = 10$ ns), implying that the retardation effects of the elastic waves between two points are negligible. Given these facts, we intuitively expect that the two friction points considered here might lead to the sliding dynamics close to the single-friction-point case as illustrated in Figs. 5. The present numerical study is to confirm this intuition, and, moreover, to reveal apparent features that are absent in the SFPM.

The temporal evolutions of the x -component elastic displacements of two friction points [see thicker solid lines in Fig. 6(b1); see the figure caption for the simulation details] exhibit features similar to the single-friction-point case. More precisely, the friction points slide rapidly in the heating period, and, then, gradually ceases their motions and converge to the centroid displacement (dashed line) in the cooling period.

However, the friction-force evolutions, as shown in Fig. 6(b2), show a feature that is absent in the SFPM. Specifically, after an initial slip ($t < 40$ ns) during which the friction forces of two points show the same direction, they turn into opposite directions. The friction force of the left point (dark blue line) is in the $-\hat{x}$ direction, while that of the right point (dark red line) is in the \hat{x} direction. The friction forces thus stretch the part of the plate between the two friction points. At the same time, the thermal contraction in the cooling period slowly drags the two points to approach each other. Finally, with the end of the thermal cooling, the friction forces remain at the same opposite nonzero values equal to the sliding resistance, while their summation vanishing (dashed line).

B. Case II

We then increase the distance between two friction points by setting that they locate with $1\text{-}\mu\text{m}$ distance to the left and right edges of the plate, respectively, as is sketched in Fig. 7(a). In this case, the distance between two points ($8 \mu\text{m}$) are comparable to the plate length, so that they can be no longer approximated as the single point as in Fig. 6. Particularly, the thermal deformations of such two points are in the opposite directions. This naturally brings one question that cannot be simply answered by referring to the insights of the SFPM: in which direction the plate should slide?

Clearly, two factors, the spatial distributions of (1) the friction forces and (2) the light absorption, are possibly involved in determining the sliding direction. To illustrate the second factor, we artificially set the absorption profile by rearranging them around two friction points with the localized energy denoted by $W_{\text{abs};1}$ (left point) and $W_{\text{abs};2}$ (right point), as is shown in Fig. 7(a). Bearing these factors in mind, we start our investigations by

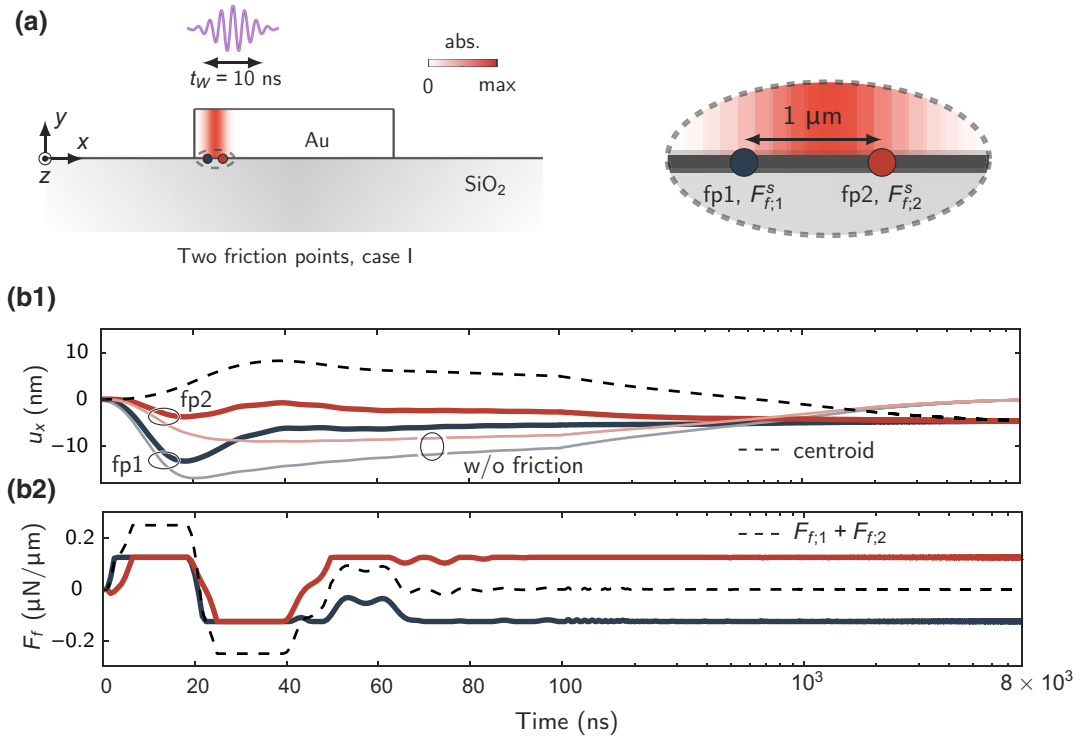


FIG. 6. Sliding dynamics with two close friction points (case I) driven by a nanosecond light pulse. (a) Sketch of the investigated problem. The right enlarged view shows two friction points with 1- μm separated distance, and the distance from the left friction point to the left edge of the plate is 0.5 μm . (b1) Temporal evolutions of x -component elastic displacements of two friction points with (dark solid lines) and without (gray solid lines) friction force, and of the centroid displacement (dashed line). (b2) Temporal evolutions of x -component friction forces of two friction points (solid lines) and their summation (dashed line). In (b1)–(b2), the friction resistances of two friction points are $F_{f,1}^s = F_{f,2}^s = 0.125 \mu\text{N}/\mu\text{m}$. The injected light pulse has $t_w = 10 \text{ ns}$ and $W_{\text{abs}} = 0.2 \text{ nJ}/\mu\text{m}$. The other simulation parameters take the same settings as the “configuration 2” in Fig. 3.

intentionally setting that the two friction points have different sliding resistances with $F_{f,1}^s = 0.1 \mu\text{N}/\mu\text{m}$ (left point) and $F_{f,2}^s = 0.15 \mu\text{N}/\mu\text{m}$, (right point), for reasons that will become clear later; the absorption profile is set with $W_{\text{abs},1} = 0.2 \text{ nJ}/\mu\text{m}$ and $W_{\text{abs},2} = 0$. The other simulation parameters are the same as in Figs. 6(b1)–6(b3).

The solid thicker lines in Fig. 7(b1) illustrate the temporal evolutions of the x -component elastic displacements of the left and right friction points, while the solid thinner lines, the same evolutions but without the friction, are also included for highlighting the roles of the friction forces. We observe that, during the heating period, the two points slide intensely in the opposite directions. Then, in the early cooling period (e.g., $20 \text{ ns} < t < 100 \text{ ns}$), their motions are significantly suppressed with negligible displacements. Then, over time ($t > 100 \text{ ns}$), the displacement of the left friction point with a smaller sliding resistance gradually approaches that of the right friction point with a larger sliding resistance, while the right friction point remains almost still. As a result, the net sliding is towards the right direction, as is confirmed by the centroid displacement [dashed line shown in Fig. 7(b1)].

We further examine the temporal evolutions of the friction forces in Fig. 7(b2). In the initial sliding phase (i.e., heating period), the friction forces of two points point in the directions opposite to the sliding directions with different magnitudes given by $F_{f,1}^s$ and $F_{f,2}^s$, respectively. Later, they gradually reverse their signs with the magnitudes approaching the smallest value of $F_{f,1}^s$ and $F_{f,2}^s$ (i.e., $F_{f,1}^s = 0.1 \mu\text{N}/\mu\text{m}$). Apparently, the friction force exerts on the right point is smaller than its sliding resistance, so that the right point is kept still by the static friction, while the left point moves towards the right side, as observed in Fig. 7(b1). Finally, in the stabilized state ($t \rightarrow \infty$), the friction forces of the left and right sides have the opposite signs and the same magnitudes of $F_{f,1}^s$ (i.e., $0.1 \mu\text{N}/\mu\text{m}$), which should lead to a small tensile stress between two points, similarly as in case I shown in Fig. 6.

The dynamic evolutions of the displacements of two friction points physically resemble the well-known game, tug of war. In the first stage, as the game starts, the competing teams stretch the rope and slide on the ground, which just mimics the sliding of two friction points in the heating period enabled by the thermal deformation.

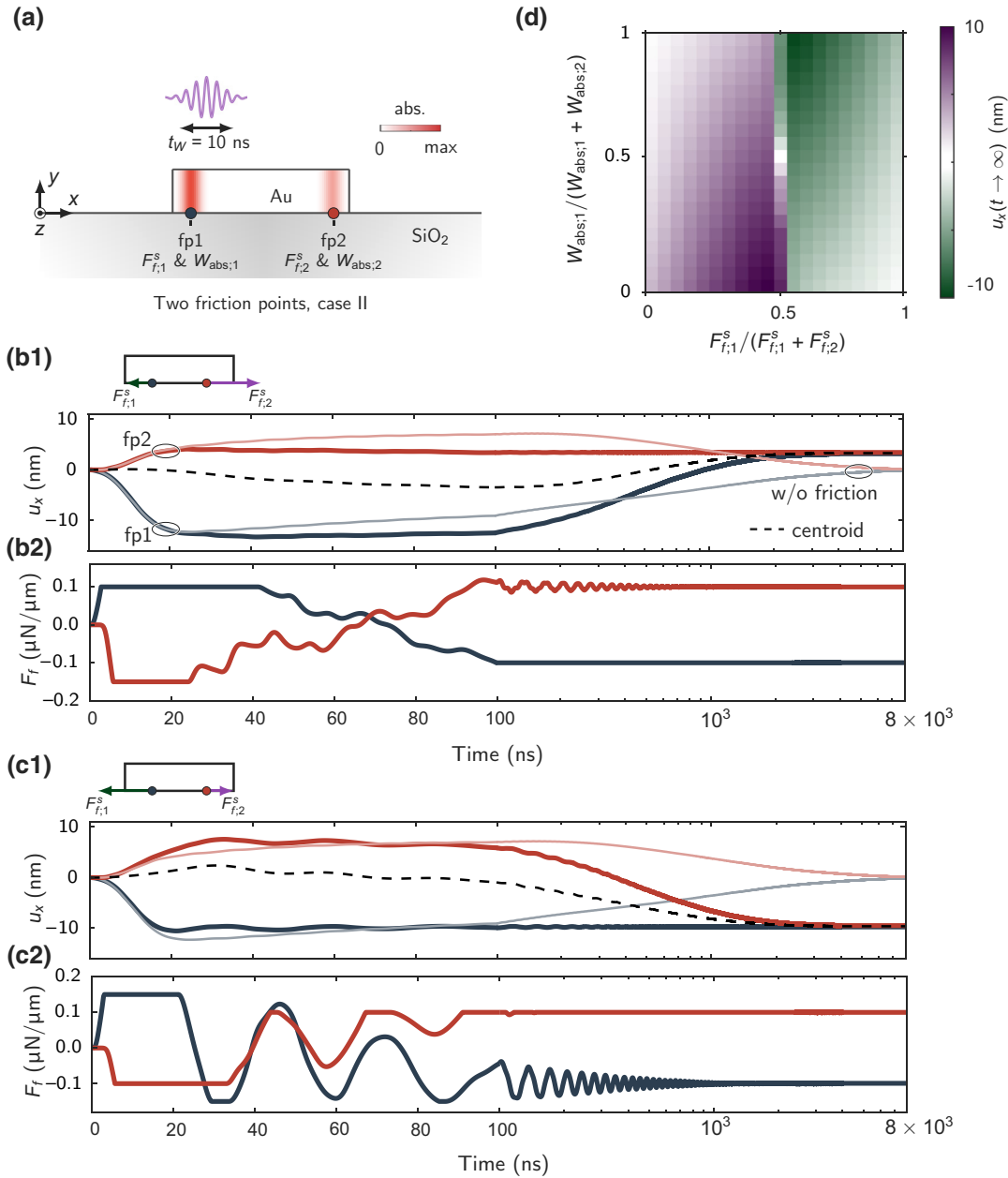


FIG. 7. Sliding dynamics with two distant friction points (case II) driven by a nanosecond light pulse. (a) Sketch of the investigated problem. Two friction points are introduced with $1\text{-}\mu\text{m}$ distance to the left and right edges of the plate. The light absorption is distributed around two friction points with localized energy denoted by $W_{\text{abs},1}$ and $W_{\text{abs},2}$. (b1) Temporal evolutions of x -component elastic displacements of two friction points with (dark solid lines) and without (gray solid lines) friction force, and of the centroid displacement (dashed line). (b2) Temporal evolutions of x -component friction forces of two friction points (solid lines) and their summation (dashed line). In (b1)–(b2), the friction resistances of two friction points are $F_{f,1}^s = 0.1 \mu\text{N}/\mu\text{m}$ and $F_{f,2}^s = 0.15 \mu\text{N}/\mu\text{m}$. The injected light pulse has $t_W = 10$ ns and $W_{\text{abs}} = 0.2 \text{ nJ}/\mu\text{m}$. The other simulation parameters take the same settings as the “configuration 2” in Fig. 3. (c1)–(c2) Same as (b1) and (b2), but with $F_{f,1}^s = 0.15 \mu\text{N}/\mu\text{m}$ and $F_{f,2}^s = 0.1 \mu\text{N}/\mu\text{m}$. (d) Net sliding distance as functions of $W_{\text{abs},1}/(W_{\text{abs},1} + W_{\text{abs},2})$ and $F_{f,1}^s/(F_{f,1}^s + F_{f,2}^s)$ with $W_{\text{abs},1} + W_{\text{abs},2} = 0.2 \text{ nJ}/\mu\text{m}$ and $F_{f,1}^s + F_{f,2}^s = 0.25 \mu\text{N}/\mu\text{m}$.

Then, the two teams adjust their body postures for larger friction against the sliding, and reach a certain static balance in a short period of time, which corresponds to the early cooling period shown in Fig. 7(b1). Eventually, the team subjected to a larger friction (e.g., due to heavier

weight or wearing shoes with firmer grip) shall drag the other team toward them and win the game, which intuitively interprets that the left friction point with a smaller sliding resistance gradually slides towards the side with a larger sliding resistance.

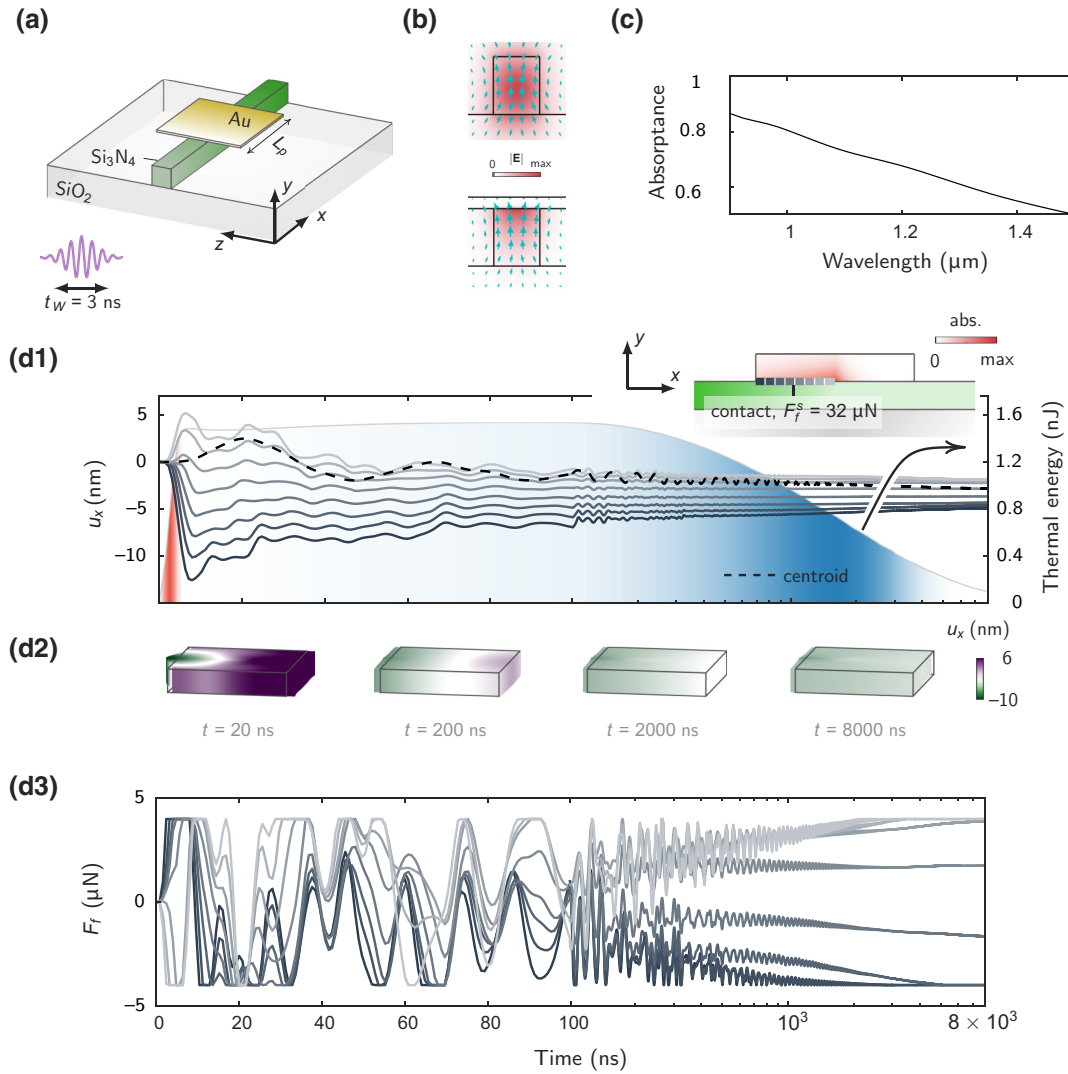


FIG. 8. Sliding of a gold plate on a Si_3N_4 nanowaveguide driven by a nanosecond light pulse. (a) Sketch of a gold nanoplate sitting above a Si_3N_4 nanowaveguide on a SiO_2 substrate. The Si_3N_4 nanowaveguide has a cross-section width of 400 nm and a height of 500 nm . The gold square plate has a slide length of $16\ \mu\text{m}$ and thickness of 100 nm . (b) Modal profiles ($|E|$ distributions) of fundamental TM mode of the Si_3N_4 nanowaveguide without (upper) and with (lower) the gold plate at light wavelength $1.03\ \mu\text{m}$. The arrows specify the directions of the in-plane E fields. (c) Absorbance spectrum of the hybrid gold- Si_3N_4 waveguide under incidence of the TM mode of the Si_3N_4 nanowaveguide. (d1) Temporal evolutions of thermal energy (shaded region) and x -component elastic displacements (solid lines). Inset: the left-half side of the plate contacting (both mechanically and thermally) with the nanowaveguide, leading to a sliding resistance of $32\ \mu\text{N}$ and a cooling time over 1000 ns . (d2) Profiles of x -component elastic displacements at different time $t = 20, 200, 2000, 8000\text{ ns}$. (d3) Temporal evolutions of x -component friction forces. In (d1) and (d3), the contact area is divided into eight equal segments, on which the averaged elastic displacements and the integrated friction forces are plotted. The temporal width and absorption energy of light pulses are $t_W = 10\text{ ns}$ and $W_{\text{abs}} = 2\text{ nJ}$, respectively.

Next, we reverse the values of $F_{f;1}^s$ and $F_{f;2}^s$ with $F_{f;1}^s = 0.15\ \mu\text{N}/\mu\text{m}$ and $F_{f;2}^s = 0.1\ \mu\text{N}/\mu\text{m}$, so that the left friction point now has a larger sliding resistance than the right point. The simulated temporal evolutions of the elastic displacements and the friction forces are plotted in Figs. 7(c1) and 7(c2), respectively. They show similar features as shown in Figs. 7(b1) and 7(b2), except that the sliding direction now reverses to the $-\hat{x}$ direction due to

the fact that the left point with a larger sliding resistance drags the right point towards it.

The comparisons between Figs. 7(b1)–7(b2) and Figs. 7(c1)–7(c2) suggest that the sliding direction is mainly determined by the friction distribution. The distribution of the light absorption, which mainly determines the strength of the thermal deformation in the early heating period, seems not to be decisive. To conclusively

evidence this observation, we compute the net displacement of the plate by varying the distribution of the absorption profile, i.e., $W_{\text{abs};1}/(W_{\text{abs};1} + W_{\text{abs};2})$ ($W_{\text{abs};1} + W_{\text{abs};2} = 0.2$ nJ/ μm), and, the friction distribution, i.e., $F_{f;1}^s/(F_{f;1}^s + F_{f;2}^s)$ ($F_{f;1}^s + F_{f;2}^s = 0.25$ $\mu\text{N}/\mu\text{m}$), and plot the results in Figs. 7(d). We see that the sliding direction (the sign of the sliding distance) is indeed determined by the relation between $F_{f;1}^s$ and $F_{f;2}^s$, and the absorption profile, parameterized by $W_{\text{abs};1}/(W_{\text{abs};1} + W_{\text{abs};2})$, is almost insignificant. More precisely, when $F_{f;1}^s > F_{f;2}^s$, i.e., the left friction dominates over the right one, the sliding direction is towards the left, and vice versa. Only in the case that $F_{f;1}^s$ and $F_{f;2}^s$ approach each other, that is, $F_{f;1}^s/(F_{f;1}^s + F_{f;2}^s)$ is close to 0.5, the sliding direction becomes dependent on the absorption distribution, which is towards the side with a larger absorption energy. Thus, these results suggest that the sliding direction is mainly determined by the friction distribution.

VII. PERSPECTIVES: A PRACTICAL PROPOSAL FOR ON-CHIP INTEGRATION

To date, all the existing experimental demonstrations of the nanosteppping motion driven by light-induced elastic waves are restricted in the microfiber-based systems (see Fig. 1). Our insights developed above can be directly applied to better interpret these experimental observations. Nevertheless, instead of going into details of the existing experiments, we here ask an unexplored question: whether the same technique can be translated onto micro- or nanowaveguide systems, or even on planar substrates. We consider that the attempts in this direction are meaningful, yet challenging in the following aspects.

First, it is known that, in a microfiber-based system, the contact between the microfiber and the micro-object is confined in a narrow line-shaped region, which results in a friction force of a few μN [29,31]. Replacing the microfiber with the micro- and nanowaveguides that generally have planar roofs increases the contact area, and, thus, enhance the friction force. To put this into concrete terms, considering that a gold plate contacts with a microfiber with a diameter of 2 μm , the effective transverse contact length (perpendicular to the axial direction of the microfiber) due to the vdW force is estimated to be in the order of 10 nm (see Fig. S1 within the Supplemental Material [41]). Then, using a nanowaveguide with a transverse width about 0.5 μm , the effective contact area is increased at least more than tenfold, so that the friction force might reach tens of μN , making the driving more challenging. Nevertheless, the insights from the previous physical modes provide some positive signs, suggesting that the use of short nanosecond pulses [e.g., with $t_w = 3$ ns, see Fig. 5(d)] is possible to enable the motion of a micro-object under the sliding resistance over 10 μN . If this is realizable, one can even imagine that a micro-object

(subjected to a friction force of tens, or even hundreds of μN) on a planar substrate might even be manipulatable with the same principle.

Second, liberating the manipulations from the microfiber-based systems can lead to wider photonic applications. For instance, in micro- and nanowaveguide systems on optical chips, if a micro-object can be delivered into user-demanded locations precisely, it could be used to control light transmission in a single waveguide, or tune power coupling between nearby waveguides, by modifying photonic environments through its movable positions. Besides, if the vibration modes of the micro-object can be additionally exploited, their combination with position manipulations might bring other possibilities in optomechanics and practical applications, such as mobile optical modulators.

Below, we provide realistic numerical simulations that positively evidence that a gold microplate can be driven by pulsed light on top of a nanowaveguide with friction force in the order of tens of μN . These simulations also echo our developed theory, and show that the revealed physical insights can be directly applied for interpreting the physics in complex systems. The design of the nanowaveguide is sketched in Fig. 8(a). A Si_3N_4 nanowire sits on a SiO_2 substrate. Both Si_3N_4 and SiO_2 have higher specific heat capacity and much lower thermal conductivity than gold (see Table S1 within the Supplemental Material [41]), thus ensuring a slow cooling process. Concretely, consider a Si_3N_4 nanowire with width 400 nm and height 500 nm, which supports single-mode propagation of the transverse-magnetic (TM) light at near-infrared wavelengths. The upper panel of Fig. 8(b) plots the modal profile of the TM waveguiding mode at 1.03 μm . Covering a gold plate on top of the Si_3N_4 nanowire, the modal energy is slightly redistributed and localized near the gold surface due to excitations of surface plasmon polaritons, as is shown in the lower panel of Fig. 8(b) (gold plate thickness and side length: 100 nm and 16 μm , respectively). As the hybrid metal-dielectric mode propagates along the nanowire, the light gradually converts into heat due to the Ohmic losses of gold, and the overall absorptance is determined by the propagation length. Accordingly, as is shown Fig. 8(c), a high absorptance (above 50%) is reached in a broad wavelength range from 0.9 μm to 1.5 μm .

To examine the actuation dynamics of the plate, we inject a nanosecond light pulse with $t_w = 3$ ns into the Si_3N_4 nanowire. The light pulse propagates along the $-\hat{x}$ direction [see the inset in Fig. 8(d1)] and leads to a total energy $W_{\text{abs}} = 2$ nJ absorbed by the plate. The plate is cut symmetrically by the nanowire in the \hat{z} direction [see Fig. 8(a)]. Moreover, taking our previous experimental experience [32] that a thin gold plate is generally curved after its transferring process onto the waveguide, we assume that only the left half side of the plate contacts with the nanowire [c.f. the inset in Fig. 8(d1)], so that the contact length in the \hat{x} direction is 8 μm , indicating

a contact area of $8 \mu\text{m} \times 400 \text{ nm}$. This area is estimated to be about ten times larger than that of the same-sized plate placed on a microfiber with $2\text{-}\mu\text{m}$ diameter (see the discussions in the second paragraph in the same section). Moreover, it is known that the friction force is linearly proportional to the contact area. Therefore, from the measured friction force in the microfiber system that is about a few μN , we reasonably set that the friction force between the plate and the nanowire is $F_f^s = 32 \mu\text{N}$.

The shaded region in Fig. 8(d1) illustrates the temporal evolutions of the thermal energy stored in the plate. It shows that, after rapid inject of the optical energy by the short light pulse, the thermal energy slowly decays with the cooling time exceeding 1000 ns . This confirms the intuition that the narrow Si_3N_4 nanowire with high heat capacity and low thermal conductivity can efficiently mitigate the heat conduction from the plate into the substrate.

The solid lines in Fig. 8(d1) show the temporal evolutions of the spatially averaged x -component elastic displacements of the eight segments that divide the contact area equally. They, in the early heating period, show noticeable differences mainly inherited from the spatial distribution of the thermal deformation. Then, they gradually approach each other, and the entire plate gains a net displacement in the $-\hat{x}$ direction [see the dashed line in Fig. 8(d1) for the centroid displacement]. This process can be better visualized in Fig. 8(d2) that shows the distributions of the x -component displacements at different time.

In the stabilized state ($t \rightarrow \infty$), the x -component displacement on the contact area shows an inhomogeneous distribution. This is similar to the simplified two-friction-points case that the displacements of the two friction points are slightly different with each other due to the “tug-of-war”-like friction stretching. The solid lines in Fig. 8(d3) show the temporal evolutions of the friction force integrated in the divided segments of the contact area, and exhibit the features similar to the two-friction-points case. Initially, the left (darker lines) and right (grayer lines) sides on the contact area experience the friction forces pointing towards the right and left sides, respectively, to resist the sliding due to the thermal deformations. Then, after rather complicated evolutions when $t > 100 \text{ ns}$, the friction forces of the two sides reverse their signs and stretch the plate.

When replacing the Si_3N_4 waveguide with a microfiber with diameter of a few μm , the transverse contact length in the z direction is reduced to tens of nanometers (see Fig. S1 within the Supplemental Material [41]). In this case, the sliding resistance is accordingly reduced. For instance, considering $F_f^s = 3.2 \mu\text{N}$ that quantitatively mimics the contact between the gold plate and the microfiber [32], the results in Fig. S4 within the Supplemental Material [41] demonstrate that the sliding shows similar features as in Fig. 8, thereby implying that the intense thermal

deformation dwarfs the impact of the different sliding resistances in the two cases. Moreover, we numerically find that the sliding is allowable even when F_f^s reaches $80 \mu\text{N}$, see Fig. S5 within the Supplemental Material [41].

To end this section, we summarize that the results in Fig. 8 encouragingly confirm that this elastic-wave-based manipulation principle is possible to be translated to micro- and nanoscale optical waveguides on optical chips.

VIII. CONCLUSIONS

In this paper, we comprehensively study the physical mechanism of nanomotion of micro-objects driven by elastic waves induced by nanosecond laser pulses. Focusing on interpreting roles of key optical-thermal-elastic quantities and parameters involved in the physical processes, including light-pulse duration and energy, thermal heating and cooling time, sliding resistance, and elastic waves, we develop a pedagogical single-friction-point model, which reveals that the use of short pulses and the thermal asymmetry in the heating and cooling timescales are two key factors to enable the motion against μN friction. Further, we discuss the effects of the friction distribution beyond the single-friction-point consideration and show the tug-of-war effects due to the friction stretching. We envision that the studied manipulating principle can be translated to micro- and nanowaveguide systems on optical chips, and provide the numerical confirmations. Our theoretical results are expected to help future developments of optical manipulation on solid interfaces [33].

ACKNOWLEDGMENTS

This project is supported by the National Natural Science Foundation of China (62275221).

-
- [1] H. Xin, Y. Li, Y. Liu, Y. Zhang, Y. Xiao, and B. Li, Optical forces: From fundamental to biological applications, *Adv. Mater.* **32**, 2001994 (2020).
 - [2] A. Ashkin and J. M. Dziedzic, Optical trapping and manipulation of viruses and bacteria, *Science* **235**, 1517 (1987).
 - [3] K. Ramser and D. Hanstorp, Optical manipulation for single-cell studies, *J. Biophotonics* **3**, 187 (2010).
 - [4] M. C. Zhong, X. B. Wei, J. H. Zhou, Z. Q. Wang, and Y. M. Li, Trapping red blood cells in living animals using optical tweezers, *Nat. Commun.* **4**, 1768 (2013).
 - [5] B. Kang, M. M. Afifi, L. A. Austin, and M. A. El-Sayed, Exploiting the nanoparticle plasmon effect: Observing drug delivery dynamics in single cells via Raman/fluorescence imaging spectroscopy, *ACS Nano* **7**, 7420 (2013).
 - [6] M. P. MacDonald, G. C. Spalding, and K. Dholakia, Microfluidic sorting in an optical lattice, *Nature* **426**, 421 (2003).
 - [7] T. Dordević, P. Samutpraphoot, P. L. Ocola, H. Bernien, B. Grinkemeyer, I. Dimitrova, V. Vuletić, and M. D. Lukin,

- Entanglement transport and a nanophotonic interface for atoms in optical tweezers, *Science* **373**, 1511 (2021).
- [8] Y. Ren, Q. Chen, M. He, X. Zhang, H. Qi, and Y. Yan, Plasmonic optical tweezers for particle manipulation: Principles, methods, and applications, *ACS Nano* **15**, 6105 (2021).
- [9] S. Awel, S. Bohne, R. Ebrahimifard, H. K. Trieu, S. Bajt, and H. N. Chapman, Optical bunching of particles in a liquid flow, *Opt. Express* **29**, 34394 (2021).
- [10] A. Ashkin, J. M. Dziedzic, J. E. Bjorkholm, and S. Chu, Observation of a single-beam gradient force optical trap for dielectric particles, *Opt. Lett.* **11**, 288 (1986).
- [11] D. G. Grier, A revolution in optical manipulation, *Nature* **424**, 810 (2003).
- [12] C. J. Bustamante, Y. R. Chemla, S. Liu, and M. D. Wang, Optical tweezers in single-molecule biophysics, *Nat. Rev. Methods Primers* **1**, 25 (2021).
- [13] H. Ren, H. Jin, J. Shu, J. Xie, E. Wang, D. A. Ge, S. Y. Tang, X. Li, W. Li, and S. Zhang, Light-controlled versatile manipulation of liquid metal droplets: A gateway to future liquid robots, *Mater. Horiz.* **8**, 3063 (2021).
- [14] L. Lin, P. S. Kollipara, A. Kotnala, T. Jiang, Y. Liu, X. Peng, B. A. Korgel, and Y. Zheng, Opto-thermoelectric pulling of light-absorbing particles, *Light: Sci. Appl.* **9**, 34 (2020).
- [15] L. Lin, M. Wang, X. Peng, E. N. Lissek, Z. Mao, L. Scarabelli, E. Adkins, S. Coskun, H. E. Unalan, B. A. Korgel, L. M. Liz-Marzán, E. L. Florin, and Y. Zheng, Opto-thermoelectric nanotweezers, *Nat. Photonics* **12**, 195 (2018).
- [16] S. Y. Park, S. Kalim, C. Callahan, M. A. Teitell, and E. P. Chiou, A light-induced dielectrophoretic droplet manipulation platform, *Lab Chip* **9**, 3228 (2009).
- [17] Z. Chen, J. Li, and Y. Zheng, Heat-mediated optical manipulation, *Chem. Rev.* **122**, 3122 (2022).
- [18] A. Terray, J. Oakey, and D. W. M. Marr, Fabrication of linear colloidal structures for microfluidic applications, *Appl. Phys. Lett.* **81**, 1555 (2002).
- [19] R. Venu, B. Lim, X. H. Hu, I. Jeong, T. S. Ramulu, and C. G. Kim, On-chip manipulation and trapping of microorganisms using a patterned magnetic pathway, *Microfluid. Nanofluidics* **14**, 277 (2013).
- [20] M. Enachi, M. Guix, V. Postolache, V. Ciobanu, V. M. Fomin, O. G. Schmidt, and I. Tiginyanu, Light-induced motion of microengines based on microarrays of TiO₂ nanotubes, *Small* **12**, 5497 (2016).
- [21] E. Hebestreit, M. Frimmer, R. Reimann, and L. Novotny, Sensing Static Forces with Free-Falling Nanoparticles, *Phys. Rev. Lett.* **121**, 063602 (2018).
- [22] G. P. Conangla, A. W. Schell, R. A. Rica, and R. Quidant, Motion control and optical interrogation of a levitating single nitrogen vacancy in vacuum, *Nano Lett.* **18**, 3956 (2018).
- [23] J. Pu, K. Zeng, Y. Wu, and D. Xiao, A miniature optical force dual-axis accelerometer based on laser diodes and small particles cavities, *Micromachines* **12**, 1375 (2021).
- [24] J. Chen, J. Ng, Z. Lin, and C. T. Chan, Optical pulling force, *Nat. Photonics* **5**, 531 (2011).
- [25] P. Arya, M. Umlandt, J. Jelken, D. Feldmann, N. Lomadze, E. S. Asmolov, O. I. Vinogradova, and S. Santer, Light-induced manipulation of passive and active microparticles, *Eur. Phys. J. E* **44**, 50 (2021).
- [26] D. Gao, W. Ding, M. Nieto-Vesperinas, X. Ding, M. Rahman, T. Zhang, C. Lim, and C.-W. Qiu, Optical manipulation from the microscale to the nanoscale: Fundamentals, advances and prospects, *Light Sci. Appl.* **6**, e17039 (2017).
- [27] K. Kendall, Adhesion: Molecules and mechanics, *Science* **263**, 1720 (1994).
- [28] W. Lyu, W. Tang, W. Yan, and M. Qiu, Light-induced in-plane rotation of microobjects on microfibers, *Laser Photonics Rev.* **16**, 1 (2022).
- [29] J. Lu, Q. Li, C.-W. Qiu, Y. Hong, P. Ghosh, and M. Qiu, Nanoscale Lamb wave-driven motors in nonliquid environments, *Sci. Adv.* **5**, 1 (2019).
- [30] J. Lu, H. Yang, L. Zhou, Y. Yang, S. Luo, Q. Li, and M. Qiu, Light-Induced Pulling and Pushing by the Synergic Effect of Optical Force and Photophoretic Force, *Phys. Rev. Lett.* **118**, 1 (2017).
- [31] S. Linghu, Z. Gu, J. Lu, W. Fang, Z. Yang, H. Yu, Z. Li, R. Zhu, J. Peng, Q. Zhan, S. Zhuang, M. Gu, and F. Gu, Plasmon-driven nanowire actuators for on-chip manipulation, *Nat. Commun.* **12**, 1 (2021).
- [32] W. Tang, W. Lyu, J. Lu, F. Liu, J. Wang, W. Yan, and M. Qiu, Micro-scale opto-thermo-mechanical actuation in the dry adhesive regime, *Light Sci. Appl.* **10**, 193 (2021).
- [33] J. Li, A. Alfares, and Y. Zheng, Optical manipulation and assembly of micro/nanoscale objects on solid substrates, *iScience* **25**, 104035 (2022).
- [34] T. P. Hunt, D. Issadore, and R. M. Westervelt, Integrated circuit/microfluidic chip to programmably trap and move cells and droplets with dielectrophoresis, *Lab Chip* **8**, 81 (2007).
- [35] X. Ding, S. C. S. Lin, B. Kiraly, H. Yue, S. Li, I. K. Chiang, J. Shi, S. J. Benkovic, and T. J. Huang, On-chip manipulation of single microparticles, cells, and organisms using surface acoustic waves, *Proc. Natl Acad. Sci. USA* **109**, 11105 (2012).
- [36] H. Ito and M. Kaneko, On-chip cell manipulation and applications to deformability measurements, *ROBOMECH J.* **7**, 3 (2020).
- [37] M. Tardif, E. Picard, V. Gaude, J. B. Jager, D. Peyrade, E. Hadji, and P. R. Marcoux, On-Chip optical nano-tweezers for culture-less fast bacterial viability assessment, *Small* **18**, 1 (2022).
- [38] Z. Zhang, C. Min, Y. Fu, Y. Zhang, W. Liu, and X. Yuan, Controllable transport of nanoparticles along waveguides by spin-orbit coupling of light, *Opt. Express* **29**, 6282 (2021).
- [39] C. Li, M. Zhang, H. Xu, Y. Tan, Y. Shi, and D. Dai, Subwavelength silicon photonics for on-chip mode-manipulation, *Photonix* **2**, 11 (2021).
- [40] J. Li, Y. Liu, L. Lin, M. Wang, T. Jiang, J. Guo, H. Ding, P. S. Kollipara, Y. Inoue, D. Fan, B. A. Korgel, and Y. Zheng, Optical nanomanipulation on solid substrates via optothermally-gated photon nudging, *Nat. Commun.* **10**, 5672 (2019).

- [41] See Supplemental Material at <http://link.aps.org/supplemental/10.1103/PhysRevApplied.19.024049> for additional numerical results and details of numerical implementations, including Refs. [44–46].
- [42] L. D. Landau, L. P. Pitaevskii, A. M. Kosevich, and E. M. Lifshitz, *Theory of Elasticity* (Butterworth-Heinemann, Oxford, England, UK, 2012).
- [43] M. Born, Quantenmechanik der stoßvorgänge, *Z. Phys.* **38**, 803 (1926).
- [44] D. Maugis, Adhesion of spheres: The JKR-DMT transition using a dugdale model, *J. Colloid Interface Sci.* **150**, 243 (1992).
- [45] P. B. Johnson and R. W. Christy, Optical constants of the noble metals, *Phys. Rev. B* **6**, 4370 (1972).
- [46] For readers who would like to know more details about the numerical method, please contact W.Y. (wyzju@gmail.com).